Characterization of a calcium phospho-silicated apatite with iron oxide inclusions

Barthélémy Desport [a,*], Joëlle Carpena [a], Jean-Louis Lacout [b], Daniel Borschneck [a], Jérôme Gattacceca [a]

[a] Centre Européen de Recherche et d'Enseignement des Géosciences de l'Environnement—CEREGE (UMR 6635), Europôle Méditerranéen de l'Arbois, BP 80, 13545 Aix-en-Provence cedex 04, France
[b] Centre Interuniversitaire de Recherche et d'Ingénierie des Matériaux—CIRIMAT (UMR 5085), ENSIACET, 4 allée Emile Monso, BP 44362, 31432 Toulouse cedex 4, France

A B S T R A C T

An iron oxide containing calcium phosphate–silicate hydroxyapatite was synthesized by calcination at 900 °C of a sample obtained by precipitation in basic aqueous solution of Ca, P, Si, Fe and Mg containing acidic solution made from dissolution of natural minerals. XRD and FTIR were used for crystallographic characterization of the main apatitic phase. Its composition was determined using ICP-AES. EDX coupled with SEM and TEM evidenced the heterogeneity of this compound and the existence of iron–magnesium oxide. Magnetic analyses highlighted that this phase was non-stoichiometric magnesioferrite ($Mg_{1.2}Fe_{1.8}O_{3.9}$) spherical nanoparticles.

Those analyses also put into evidence the role of calcination in synthesis. Carbonates detected by FTIR and estimated by SEM-EDX in non-calcinated sample were removed from apatitic structure, and crystallization of apatite was enhanced during heating. Moreover, there was phase segregation that led to magnesioferrite formation.

Keywords:
B1. Phosphates
B1. Calcium compounds
B1. Nanomaterials
B2. Magnetic materials

1. Introduction

Apatites form a large family of isomorphous minerals with the general chemical formula $Me_{10}(XO_4)_6Y_2$, where Me represents a cation and XO_4 and Y represent anionic groups. A well-known representative member of the apatite group is calcium phosphate hydroxyapatite (HAp) $Ca_{10}(PO_4)_6(OH)_2$. One of the main characteristics of the apatite structure is that it allows a large number of substitutions at all three sites (Me, X and Y). Coupled substitutions frequently occur when one ion is replaced by another of the same sign but of different charge. Neutrality is maintained by substitutions of ions with dissimilar charges or vacancies elsewhere [1]. The other main properties of the apatite structure are its high resistance to chemical corrosion in neutral-to-alkaline environments, its weak and retrograde solubility and its potential for restoring self-irradiation damages. Because of this, apatite has been used in applications such as biomaterials [2], chromatography [3], sensors [4], detoxification of wastes and water [5] and for the immobilization of hazardous heavy metals [6] and radioactive wastes [7].

The introduction of silicon in HAp is of interest in several applications. For instance, HAp is widely used in medical fields due to its good biocompatibility, bioactivity, high osteoconductive and/or osteo-inductive non toxicity, non inflammatory behavior and non immunogenicity properties [8], and incorporation of silicates in the HAp lattice is considered to be a potential method for improving the bioactivity of HAp [9]. Silicate apatites have also been proposed as potential matrices for actinides conditioning [10]. As a matter of fact, such apatites are found in geological media. These minerals called britholites were detected in the natural nuclear reactor (Oklo) without corrosion or irradiation damage [11].

Several synthesis routes can be used to prepare silicon-substituted hydroxyapatites such as sol–gel methods [12], hydrothermal methods [13,14], solid state co-substituted methods [15,16] and aqueous precipitation at high pH [17].

Hydroxyapatite with a hexagonal structure in the space group $P6_3/m$ has anisotropic magnetic properties [18], so the crystal growth may be influenced under external high magnetic fields [19,20]. Magnetic fields have been used not only to control the grain orientation of hydroxyapatite, but also to improve the biological activity of biomaterials [21]. It is reasonable to speculate that the local magnetic field produced by magnetic particles can influence the growth of apatite crystals and the bioactivity of materials. Moreover, magnetic particles with good biocompatibility have been developed as thermoseeds for hyperthermia treatment of bone tumors under an oscillating magnetic field [22]. In addition, small magnetic particles are of particular interest since they show properties different from those of bulk materials [23]. Such magnetic materials lead to technological applications in ferrofluids, catalysts and also in magnetic recordings. Finally, iron oxides are well known for their applications in water detoxification

* Corresponding author. Tel.: +33 4 42 97 17 76; fax: +33 4 42 97 15 05.
E-mail address: desport@cerege.fr (B. Desport).

doi:10.1016/j.jcrysgro.2010.12.054

[24,25]. This can be added to apatite depollution abilities: if iron oxides could be included in apatite materials, it would allow addition of the iron oxide depollution properties to those of apatites. Several authors show that they obtain apatite with iron-rich phases dispersed into the crystals. These iron-rich phases have been described as hematite α-Fe_2O_3 [26], magnetite Fe_3O_4 [27] or brownmillerite $Ca_2Fe_2O_5$ [28].

In this work we will investigate a silicate apatite with small iron-rich ferrimagnetic phases synthesized by basic aqueous precipitation. The aim is to characterize crystallography and chemistry of the different phases composing the obtained material.

2. Experimental procedure

2.1. Synthesis

An acidic solution was prepared with Ca, P, Fe, Mg and Si by dissolution of natural apatite and natural iron and magnesium containing silicates in hydrochloric acid (1 mol L^{-1}). The atomic ratio Ca/P is close to 1.67, which corresponds to that of stoichiometric hydroxyapatite. The average concentrations of Ca, P, Fe, Mg and Si in this liquid are 61%, 28%, 5%, 2% and 4%wt, respectively. The preparation of this solution is going to be patented (procedure in progress) and will not be detailed further.

The solution was added drop-by-drop to sodium hydroxide (1 N) with twice as much sodium hydroxide than the added liquid and stirred for 3 h. This formed a white precipitate that gradually became reddish. This precipitate was recovered by filtration, washed with MilliQ water then dried at room temperature for 24 h. This red precipitate will be denominated as "non-calcinated sample". The final compound was obtained by calcination in air at 900 °C for 1 h and will be denominated as "synthesized material".

2.2. Method of characterization of solid sample

The samples were examined by X-ray diffraction (XRD) at room temperature on a PANalytical X'pert Pro diffractometer using $K_\alpha Co$ radiation (λ=1.79 Å) at 40 kV and 40 mA. Data were collected by the step-counting method (step size 0.033°) between 5° and 90° (2θ) with a counting time of 4.5 s per step.

Fourier transformed infrared spectra (FTIR) were recorded at room temperature on a Bruker Equinox 55 with the KBr pellet technique. A hundred scans were collected and averaged with a range of 4000–400 cm^{-1} and a resolution of 4 cm^{-1}.

For the analysis by ICP-AES, the compounds were mixed with lithium metaborate 99.9%, then fused at 1000 °C for 25 min and dissolved into HCl (0.6 M). ICP-AES measurements were made using a JY-Horiba Ultima-C spectrometer. Ca, P, Fe, Mg and Si were analyzed. The carbonate determination was calculated by percentage weight loss after heating at 1000 °C.

The elemental composition was also measured by energy dispersive X-ray spectroscopy (EDX) OXFORD INCA coupled with scanning electron microscope (SEM) FEI XL30 SFEG. Twenty EDX scans were collected and averaged.

Structural observations of samples were performed by transmission electron spectroscopy (TEM) with electron diffraction (ED) and energy dispersive X-ray spectroscopy (EDX) using JEOL JEM 2010F.

Magnetic susceptibility measurements and thermomagnetic analyses were performed with an Agico MFK1-FA apparatus. Hysteresis loops were studied with a Princeton Micromag Vibrating Sample Magnetometer (VSM). Those analyses were made on the KBr pellets used for FTIR.

3. Results

3.1. X-ray diffraction

Fig. 1 presents the XRD pattern of the synthesized material. Synthetic hydroxyapatite pattern (JCPDS: 00-009-0432) is easily identified: the main phase of the product is an apatitic phase. A minor phase appears: lines at 35.1° and 50.4° (corresponding to a distance of 2.96 and 2.10 Å) fit with magnetite (Fe_3O_4; JCPDS: 00-019-0629), magnesioferrite ($MgFe_2O_4$; JCPDS: 00-036-0398) or periclase (MgO; JCPDS: 00-045-0946).

Lattice parameters of synthesized material were calculated from X-ray diffractogram with Checkcell software, based on pure hydroxyapatite lattice parameters: a=9.4176 Å; c=6.8814 Å [1]. The calculated parameters are: a=9.4075 Å; c=6.8955 Å. Those parameters lightly differ from theoretical hydroxyapatite lattice parameters. In addition, theoretical hydroxyapatite lattice volume is 528.55 $Å^3$ and calculated sample lattice volume is 528.50 $Å^3$. The lattice volume is the same.

Non-calcinated sample has a badly defined XRD pattern (Fig. 2). However, the shape of this diffractogram fits quite well with the synthetic hydroxyapatite phase pattern.

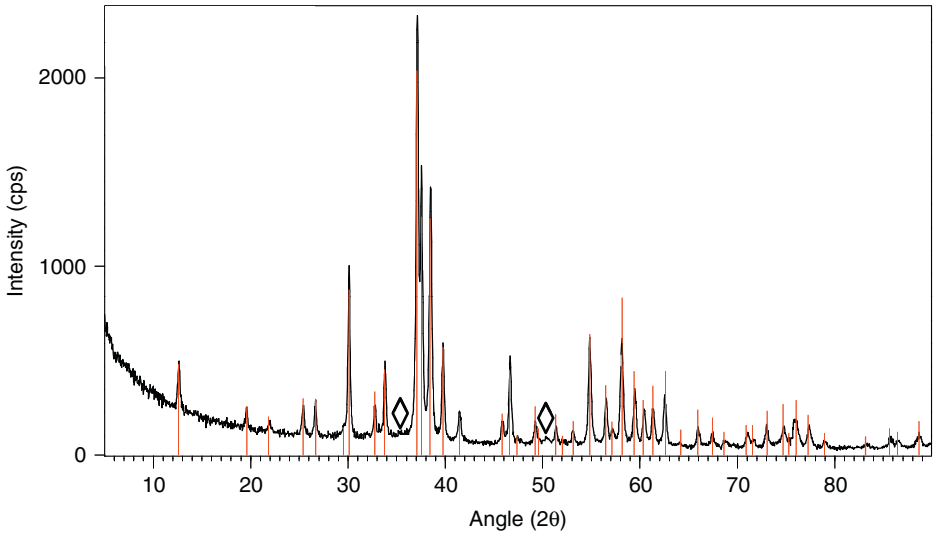

Fig. 1. XRD pattern of synthesized material. All the diffraction lines correspond to calcium hydroxyapatite (JCPDS : 00-009-0432), except those marked ◇.

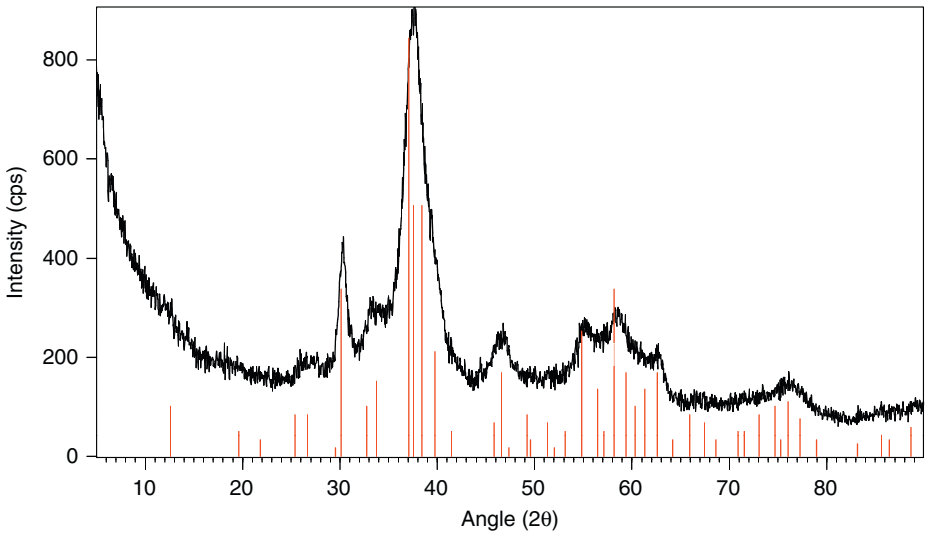

Fig. 2. XRD pattern of non-calcinated sample. Pattern of pure calcium hydroxyapatite (JCPDS: 00-009-0432) is added.

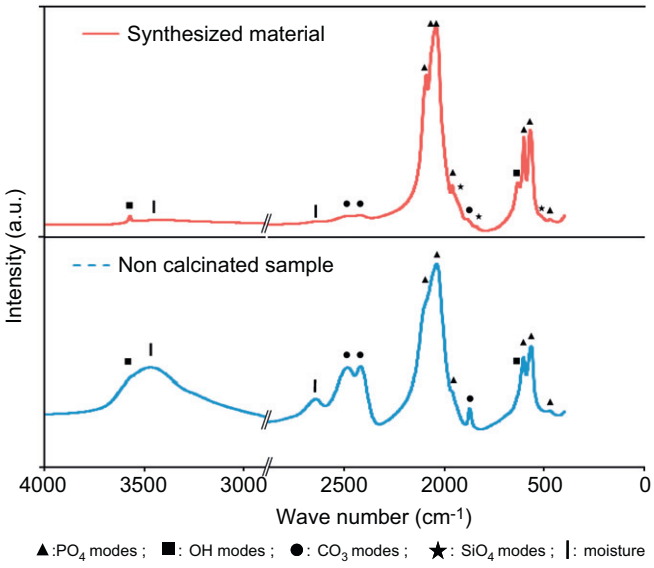

Fig. 3. FTIR spectra of synthesized material (up) and non-calcinated sample (down).

3.2. *Infrared spectroscopy*

Fig. 3a shows the FTIR spectrum of synthesized material. Table 1 summarizes the observed infrared modes.

Many bands in this spectrum correspond to PO_4 vibrational modes. The ν_3 PO_4 mode is the most intense and appears as a very strong band at $\sim$1040 cm^{-1}, a shoulder at $\sim$1068 cm^{-1} and a strong band at $\sim$1092 cm^{-1}. All PO_4 modes confirm that the main phase of synthesized material is apatite [1].

The bands at 3570 and 634 cm^{-1} are assigned to the OH stretching and the OH librational modes, respectively, in the hydroxyapatite structure [1]. In addition, seven shoulder bands located between 950 and 400 cm^{-1} appear in this spectrum. According to Boyer et al. [15] and Gibson et al. [17], those bands can all be assigned to SiO_4 vibrational modes in apatite.

Finally, this sample presents a very weak doublet band at about 1483 and 1420 cm^{-1} and a singlet band at 874 cm^{-1}. Those bands are assigned to ν_3 asymmetric stretch vibration and ν_2 out-of-plane bend vibration of B-type CO_3, respectively, in the apatitic structure [29].

A study of FTIR spectrum of non-calcinated sample (Fig. 3b, Table 1) shows that intensity of carbonate bands is stronger than that in synthesized material. On the contrary, intensity of bands assigned to PO_4 and OH vibrational modes decreases and some bands attributed to PO_4 do not appear. Finally, bands corresponding to SiO_4 are not detected.

Table 1
Room temperature observed IR modes and their assignments.

Synthesized material	Non-calcinated sample	Assignment
3600–2800br	3600–2800br	Moisture
3570w	3570sh	OH vibration
1639vw	1641m	Moisture
1492w	1483s	ν_3 CO_3
1420w	–	–
1092s	1095sh	ν_3 PO_4
1068sh	–	–
1045vs	1038vs	–
961m	962w	ν_1 PO_4
947sh	–	SiO_4 vibration
926sh	–	–
891sh	–	–
878sh	874m	ν_2 CO_3
843sh	–	SiO_4 vibration
633m	635sh	OH vibration
602s	606s	ν_4 PO_4
571s	567s	–
521sh	–	SiO_4 vibration
503sh	–	–
473w	473w	ν_2 PO_4
461sh	–	–
417sh	–	SiO_4 vibration

Codes: vs: very strong, s: strong, m: medium, w: weak, vw: very weak, sh: shoulder, br: broad band.

3.3. *ICP-AES*

Table 2a presents the average composition in weight percentage of ICP-AES analysis made for synthesized material with the relative standard deviation (RSD).

An apatite $Me_{10}(XO_4)_6Y_2$ is stoichiometric if the ratio between metallic cation (Me) and polyhedral anion (X) is 1.67. Considering Ca, P and Si, a theoretical composition of synthesized material estimated by ICP-AES is presented in Table 2b (the total number of PO_4 and SiO_4 ions was fixed to 6, according to the fact that tetrahedral sites do not accept vacancies). According to this table, Ca/(P+Si) ratio (1.672) is very close to stoichiometric ratio.

Since carbon was used in the protocol, this element was not measured by ICP-AES but by weight loss after calcination at 1000 °C. The estimated quantity of carbon present in this material is 0.47%wt.

3.4. SEM-EDX investigation

Table 3a presents the average composition of EDX scans made for synthesized material and for non-calcinated sample with the relative standard deviation (RSD). Since carbon was used to metalize samples, this element was not measured. It can be noticed that, according to RSD of each element, the synthesized material is not homogeneous. It confirms that this material is not single phase and that minor phases can be found in this material. On the contrary, the sample before calcination is more homogeneous. A theoretical composition of non-calcinated sample estimated by SEM-EDX is presented in Table 3b (the total number of PO_4, SiO_4 and CO_3 ions was fixed to 6, according to the fact that tetrahedral sites do not accept vacancies).

3.5. TEM study

Low-magnification TEM image and electronic diffraction pattern of synthesized material are shown in Fig. 4. This material is porous and heterogeneous; some dense, spherical particles appear

Table 2a
Weight composition of synthesized material obtained by ICP-AES.

Element	Ca	P	Fe	Mg	Si	C	Total
Average (%wt)	63.82	27.38	4.61	1.80	1.92	0.47	100
RSD%	1.54	8.81	3.57	1.45	2.16	3.72	–

Table 2b
Theoretical composition of synthesized material (calculated from ICP-AES, in number of groups per lattice).

Group	Ca	PO_4	SiO_4	Y	Ca/(P+Si)
Number/lattice	10.03	5.57	0.43	1.63	1.672

Table 3b
Theoretical composition of non-calcinated sample (calculated from SEM-EDX, in number of groups per lattice).

Group	Ca	PO_4	SiO_4	CO_3	Y	Ca/(P+Si+C)
Number/lattice	9.97	5.25	0.34	0.41	2.00	1.661

Table 3a
Massic composition found by SEM-EDX

	O	Ca	P	Fe	Mg	Si	Na	Total
Synthesized material (%wt)								
1	29.53	43.82	17.48	4.33	1.14	1.04	2.67	100
2	32.22	41.96	16.87	3.42	1.26	1.08	3.19	100
3	22.45	52.85	16.75	5.52	0.46	0.79	1.18	100
4	27.92	46.48	18.37	3.63	1.10	1.09	1.41	100
5	41.58	32.92	14.82	3.51	1.07	1.17	4.93	100
6	47.62	28.06	13.39	2.71	1.24	0.89	6.09	100
7	39.46	38.91	15.66	2.43	0.55	0.62	2.37	100
8	50.26	28.50	12.54	2.73	1.03	0.86	4.08	100
9	44.60	30.96	13.15	4.57	0.88	1.13	4.71	100
10	41.46	33.27	14.22	4.30	1.38	1.11	4.27	100
11	50.51	28.80	13.07	2.43	0.98	0.94	3.28	100
12	50.54	30.01	13.06	2.33	0.79	0.74	2.52	100
13	45.84	32.52	14.22	2.68	0.63	0.91	3.20	100
14	38.24	38.53	15.41	2.97	0.88	0.94	3.02	100
15	47.09	32.74	14.36	1.98	0.00	0.89	2.94	100
16	43.31	33.92	15.19	2.65	0.56	1.05	3.33	100
17	39.78	34.38	15.46	3.67	1.05	1.26	4.39	100
18	55.80	25.70	11.85	1.81	0.76	0.60	3.48	100
Average (%wt)	41.57	35.24	14.77	3.21	0.88	0.95	3.39	100.00
RSD (%)	21.35	20.42	12.19	30.97	39.11	19.24	35.89	–
Non-calcinated sample (%wt)								
1	40.44	36.40	15.51	2.19	0.54	0.92	4.01	100.00
2	32.01	42.31	16.99	4.09	0.80	0.99	2.82	100.00
3	29.44	45.42	16.75	4.26	0.70	0.95	2.49	100.00
4	36.09	40.29	15.39	3.91	0.49	0.85	2.98	100.00
5	32.35	42.28	17.13	3.42	0.87	0.83	3.12	100.00
6	41.24	35.32	14.95	3.17	0.90	0.89	3.53	100.00
7	35.90	37.94	16.05	4.58	0.90	1.16	3.47	100.00
8	37.19	37.45	15.63	4.46	0.85	0.80	3.62	100.00
9	40.29	36.30	14.82	3.78	0.62	0.60	3.60	100.00
10	39.07	36.84	14.85	3.96	0.97	1.01	3.30	100.00
11	31.46	43.94	16.23	3.44	1.13	1.40	2.40	100.00
12	36.10	38.66	16.15	3.96	1.25	0.95	2.94	100.00
13	39.19	35.29	16.00	3.44	1.26	0.84	3.98	100.00
14	35.29	39.40	16.93	3.41	0.60	1.10	3.25	100.00
15	36.70	38.90	15.53	3.95	0.92	0.81	3.20	100.00
16	38.54	37.20	15.00	4.04	1.10	1.06	3.06	100.00
17	42.11	35.78	14.44	2.23	0.91	0.50	4.03	100.00
18	38.48	36.21	15.54	3.53	1.22	1.25	3.77	100.00
Average (%wt)	36.49	38.95	15.87	3.57	0.88	0.92	3.31	100.00
RSD (%)	9.74	7.88	5.26	18.87	26.52	22.74	13.97	–

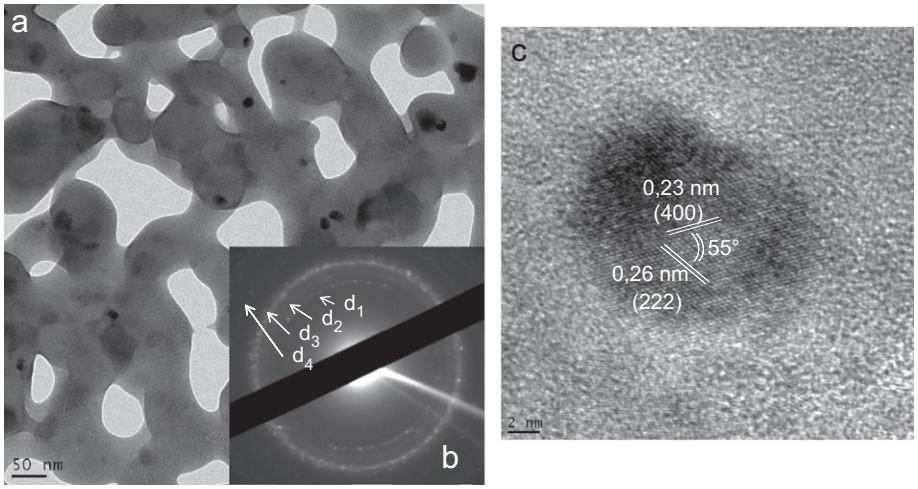

Fig. 4. TEM low-magnification image (a), electronic diffraction (b) and high-magnification image (c) of synthesized material.

Table 4
TEM-EDX qualitative analysis on synthesized material.

		Ca	P	Fe	Mg	Si	Total
Analysis (%wt)							
1	Centered	47.30	26.01	7.46	14.97	4.26	100
	Next	42.26	49.28	2.08	−1.20	7.58	100
2	Centered	36.25	39.47	19.71	1.62	2.95	100
	Next	52.05	42.07	0.44	−1.69	7.14	100
3	Centered	43.54	34.91	14.74	2.73	4.08	100
	Next	47.26	42.15	0.75	0.91	8.94	100
4	Centered	37.40	25.43	28.06	5.98	3.14	100
	Next	51.39	43.28	1.90	−0.39	3.83	100
5	Centered	41.88	38.00	11.60	2.99	5.53	100
	Next	48.80	45.47	1.80	0.13	3.79	100
6	Centered	12.75	24.56	38.85	19.95	3.90	100
	Next	52.37	40.42	2.85	0.63	3.74	100
7	Centered	25.88	20.48	38.40	9.91	5.33	100
	Next	53.24	37.78	2.32	−0.29	6.95	100
Analysis (%at)							
1	Centered	40.41	28.76	4.58	21.07	5.18	100
	Next	36.31	54.84	1.26	−1.71	9.30	100
2	Centered	33.47	47.14	13.06	2.45	3.88	100
	Next	45.58	47.68	0.27	−2.45	8.92	100
3	Centered	39.73	41.21	9.65	4.10	5.31	100
	Next	40.56	46.77	0.46	1.27	10.94	100
4	Centered	35.69	31.42	19.22	9.37	4.30	100
	Next	45.23	49.31	1.20	−0.54	4.80	100
5	Centered	37.32	43.81	7.43	4.40	7.04	100
	Next	42.59	51.36	1.13	0.19	4.74	100
6	Centered	11.50	28.67	25.15	29.66	5.02	100
	Next	46.32	46.25	1.82	0.89	4.71	100
7	Centered	24.92	25.51	26.53	15.73	7.32	100
	Next	47.03	43.18	1.48	−0.43	8.73	100

within the material. The electronic diffraction pattern indicates visible diffraction rings. The interplanar spacings (d_1=3.5 Å; d_2=3.2 Å; d_3=2.9 Å; d_4=2.3 Å) are in agreement with the characteristic spacings of hydroxyapatite.

High-magnification images (Fig. 4c) clearly show the dense particles in the synthesized material, with an approximate size of 5–20 nm. A study of crystalline structure of those dense particles through high-magnification images shows two main families of planes. The interreticular distances are 0.23 and 0.26 nm, respectively, and the angle between the two families of planes is 55°. This corresponds to planes (4 0 0) and (2 2 2) of magnetite and magnesioferrite structures.

Table 4 presents EDX qualitative analysis of synthesized material around the dense particles detected by high-magnification images. Each analysis compares a measurement centered on a particle and a measurement outside the particle on the apatite. A graphic illustration of analysis #7 is shown on Fig. 5. It appears that Ca, P, Si, Fe and Mg are detected when the analysis is centered on a particle. When a measurement is made in the apatite next to the same particle, Ca, P and Si are still detected; Fe and Mg are not detected in the apatitic phase.

Fig. 6 shows low-magnification TEM image (a), electronic diffraction pattern (b) and high-magnification TEM image (c) of non-calcinated sample. Many light-shaded spots within the sample indicate the presence of a mesoporous structure. Moreover, the non-calcinated sample seems to be homogeneous in all the material. The diffraction rings in electronic diffraction pattern are less visible but indicates the presence of an apatitic phase. The high-magnification image shows that non-calcinated sample appears as a nanocrystallized material where nanodomains are oriented in all directions. It is difficult to estimate the size of those nanodomains. This confirms that a minor phase was formed and that the apatitic phase was better crystallized after calcination. Finally, EDX qualitative analysis of non-calcinated sample (Table 5) shows that before calcination, the sample is homogeneous for all detected elements (Ca, P, Si, Fe, Mg).

3.6. Magnetism

The hysteresis loop measured for synthesized material with a VSM (Fig. 7) shows that this compound contains a ferromagnetic phase. The coercive force (B_c=16 μT) and the ratio of remanent magnetization at saturation (7.8 nAm^2) to saturation magnetization (1.25 μAm^2) are very low, which shows that the ferromagnetic fraction is mostly superparamagnetic, i.e. unable to carry a magnetic remanence.

Magnetic saturation in synthesized material occurs at ~150 mT, which is compatible with magnetite (Fe_3O_4) and maghemite (γ-Fe_2O_3) and excludes most other common ferromagnetic minerals (hematite, goethite, pyrrhotite, etc.). However, maghemite is not stable at a temperature higher than 600 °C [30], and would not be present after calcination at 900 °C. The ferromagnetic fraction is presumably a substituted magnetite. Since Mg was detected by TEM study of the dense nanoparticles, this magnetite is probably substituted by magnesium.

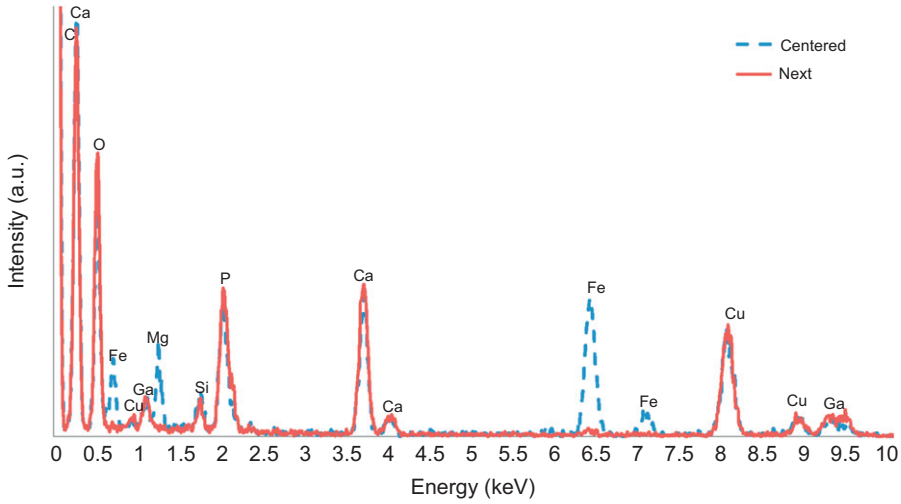

Fig. 5. EDX spectra of synthesized material, centered on a ferric particle and next to the same particle on apatitic matrix. Cu and Ga are brought by sample preparation protocol.

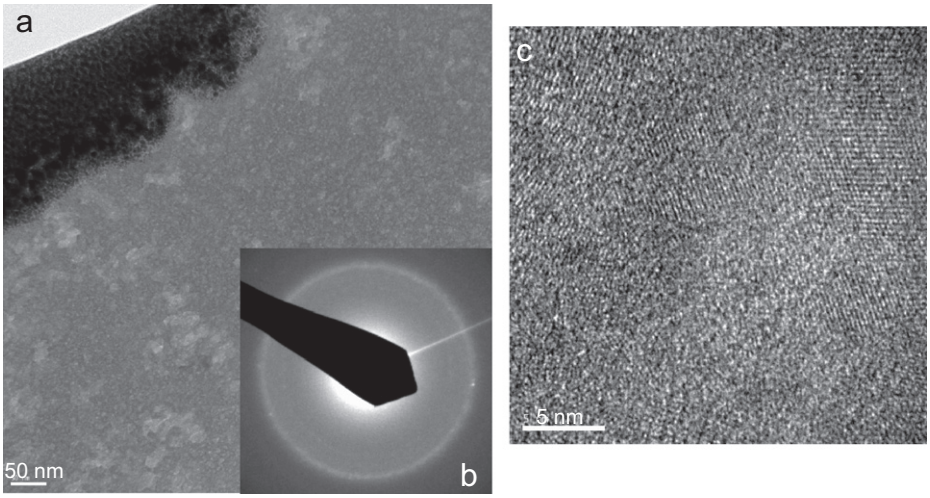

Fig. 6. TEM low-magnification image (a), electronic diffraction (b) and high-magnification image (c) of non-calcinated sample.

Fig. 8 shows the magnetic susceptibility as a function of the temperature (thermomagnetic analyses), which is used to determine the Curie temperature of the ferromagnetic minerals. The synthesized material has a Curie temperature of ~220 °C. This value corresponds neither to stoichiometric magnetite (T_C= 585 °C) nor magnesioferrite ($MgFe_2O_4$) (T_C=440 °C). However, Wirtz and Fine [31] showed that the Curie temperature of non-stoichiometric magnesioferrite $Mg_xFe_{3-x}O_{4-(x-1)/2}$ decreases when x increases. The Curie temperature of calcinated sample is compatible with x=1.2 [31]. Therefore the ferromagnetic phase contained in the synthesized material is $Mg_{1.2}Fe_{1.8}O_{3.9}$.

It is possible to estimate the proportion of superparamagnetic particles by measuring the magnetic susceptibility at different frequencies (976, 3904 and 15,616 Hz in this study). Indeed, magnetic susceptibility will decrease with increasing frequency if superparamagnetic particles are present. For synthesized material, magnetic susceptibility decreases by 27% between 976 and 15,616 Hz. This indicates that almost all $Mg_{1.2}Fe_{1.8}O_{3.9}$ particles are slightly below the ferromagnetic/superparamagnetic size limit, which is around 25 nm for magnetite [32].

Since saturation magnetization is strictly proportional to the content of ferromagnetic mineral, the amount of $Mg_{1.2}Fe_{1.8}O_{3.9}$ crystallized in synthesized material can be quantified if the saturation magnetization of pure $Mg_{1.2}Fe_{1.8}O_{3.9}$ is known. This latter value can be estimated to 40 Am^2/kg [31]. The mass-normalized saturation magnetization calculated from hysteresis loop (Fig. 7) is 0.405 Am^2/kg, which corresponds to an amount of ~1%wt of non-stoichiometric magnesioferrite ($Mg_{1.2}Fe_{1.8}O_{3.9}$) in the synthesized material.

4. Discussion

4.1. Synthesized material

The main phase of the synthesized material is an apatite, as it clearly appears on XRD. Moreover, this phase is a silicate apatite, as silicate bands appears on FTIR spectrum. Infrared spectrum also shows the presence of OH groups. The inclusion of silicon into the apatitic structure was confirmed by TEM-EDX, since this element is homogeneous in the entire sample. In addition, TEM-EDX also highlights the homogeneous repartition of calcium in this material. The synthesized material is a well crystallized phosphate–silicate calcium hydroxyapatite.

When silicate groups are introduced in apatitic structure, a and c lattice parameters both increase [15]. In the case of synthesized

material, the decrease in a parameter can be explained by the presence of vacancies in the channels [1]. This is consistent with theoretical composition of this material (Table 2b). B-type carbonates detected by FTIR also have an influence on lattice parameters: *a* parameter decreases and *c* parameter increases [33]. However, the calculated amount of carbonates is small and their contribution in lattice parameters variations is very low in comparison with silicates.

EDX coupled with SEM showed that Ca, P, Fe, Mg and Si are found in the whole sample, but this material is heterogeneous. If Ca, P and Si are considered into the structure, ICP-AES analysis showed that the ratio Me/X is close to 1.67; this shows that synthesized material is a phosphate–silicate calcium hydroxyapatite. Carbonates were not considered in tetrahedral sites because of their very low contribution estimated by lattice parameters study. They are probably in a separate phase undetected by the used techniques. Iron and magnesium were not included in theoretical calculated apatite structure; almost all cationic sites were occupied by calcium.

TEM high-magnification images and EDX highlighted the presence of nanocrystallized magnesioferrite phase in synthesized material. This was confirmed by magnetic analyses, which also indicated that this magnetic mineral is not stoichiometric ($Mg_{1.2}Fe_{1.8}O_{3.9}$) and represent ~1%wt of the whole material. 1%wt is the limit of detection by XRD; this proves that $Mg_{1.2}Fe_{1.8}O_{3.9}$ was the detected minor phase in the synthesized material XRD pattern.

It can be noticed that TEM-EDX qualitative analysis of the synthesized material did not detect iron and magnesium in the apatitic phase. This shows that there was phase segregation during the synthesis, and most part of iron and magnesium formed magnesioferrite. However, the presence of iron and magnesium in the main phase still has to be proved, as the used analyses were not precise enough to detect those elements in the apatitic phase.

Table 5
TEM-EDX qualitative analysis on non-calcinated sample.

	Ca	P	Fe	Mg	Si	Total
Analysis (%wt)						
1	56.03	21.79	15.56	2.46	4.15	100
2	58.93	23.12	12.25	2.08	3.61	100
3	60.22	24.06	10.38	1.73	3.62	100
4	59.65	23.43	11.18	1.97	3.76	100
5	56.76	22.28	15.55	1.78	3.62	100
6	60.21	22.25	13.09	1.44	3.01	100
7	59.47	22.53	13.41	1.48	3.10	100
8	58.05	21.90	15.01	1.70	3.33	100
9	58.72	23.32	13.30	1.32	3.35	100
10	59.72	21.76	13.84	1.16	3.53	100
11	59.59	22.41	13.27	1.41	3.32	100
12	59.35	22.30	13.56	1.56	3.24	100
13	60.12	22.37	12.31	1.40	3.80	100
Analysis (%at)						
1	53.17	26.76	10.59	3.85	5.62	100
2	55.47	28.17	8.28	3.23	4.85	100
3	56.38	29.16	6.97	2.66	4.83	100
4	55.95	28.44	7.52	3.04	5.05	100
5	54.12	27.49	10.64	2.81	4.93	100
6	57.31	27.40	8.95	2.26	4.08	100
7	56.57	27.73	9.15	2.34	4.21	100
8	55.43	27.06	10.29	2.67	4.54	100
9	55.72	28.63	9.05	2.06	4.53	100
10	57.01	26.87	9.48	1.83	4.82	100
11	56.66	27.58	9.06	2.20	4.50	100
12	56.47	27.45	9.25	2.44	4.39	100
13	56.90	27.40	8.36	2.19	5.14	100

4.2. *Effects of calcination*

Differences between non-calcinated sample and synthesized material give information about calcination effects.

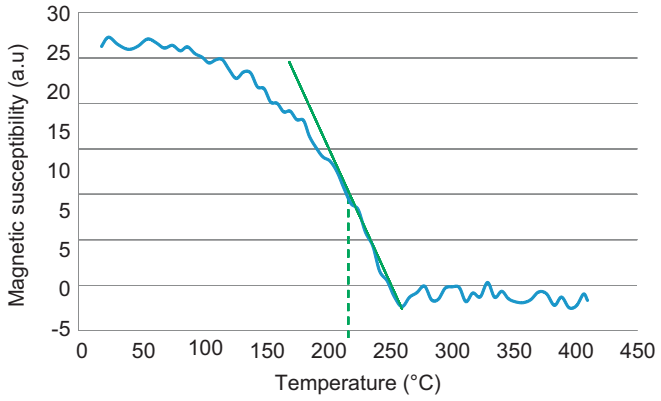

Fig. 8. Magnetic susceptibility of synthesized material as a function of the temperature. Estimated Curie temperature: 220 °C.

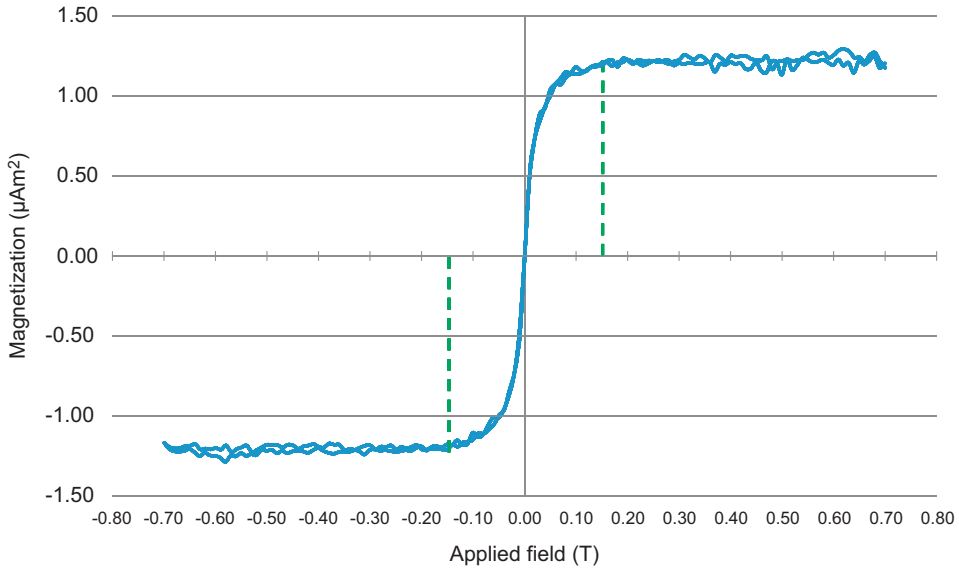

Fig. 7. Magnetization of synthesized material as a function of the applied field measured at 298 K. Magnetic saturation occurs at ~150 mT.

The fact that non-calcinated sample diffractogram fits well with pure hydroxyapatite pattern and that the electron diffraction pattern of this sample shows diffraction rings fitting with apatite interplanar spacings, proves that apatite is the main phase of this sample. FTIR spectrum highlights the presence of PO_4 and OH groups, which confirms the presence of phosphate hydroxyapatite. TEM high-magnification image of this sample shows crystallized domains polyoriented at the nanoscale, thus non-calcinated sample is nanocrystalline. Crystallization occurs during calcination with the apatite nanodomains growth.

FTIR puts into evidence the presence of carbonates in the apatitic structure of non-calcinated sample. Indeed, B-type carbonate bands are very strong in this spectrum. Moreover, the decrease in the intensity of the bands corresponding to OH modes is related to high carbonate content in the apatitic structure [34]. In addition, the bands in the ν_3 PO_4 region broaden and become less intense, which can be explained by the presence of carbonates [35]. After calcination, the intensity of carbonates bands decreased; B-type carbonates were removed from the apatitic structure remaining in the sample mainly as A-type carbonates in channels.

Although silicate bands are not detected in the non-calcinated sample FTIR spectrum, EDX coupled with either a SEM or a TEM showed that Ca, P, Fe, Mg and Si are homogeneous in the whole sample. Moreover, the ratio Me/X is close to 1.67 only if Ca, P, Si and B-type carbonates are considered. This sample is a phosphate–silicate–carbonate calcium hydroxyapatite. All cationic sites are occupied by calcium, thus introduction of iron or magnesium in the apatitic structure is not considered.

EDX coupled with TEM shows that non-calcinated sample is homogeneous for all detected elements. It also highlights that synthesized material contains magnesioferrite particles and that neither iron nor magnesium is detected in the apatite main phase. This shows that calcination induces phase segregation. The precise form of iron and magnesium in non-calcinated sample is still to understand. These two elements either form non-magnetic particles that are too small for the TEM to be detected or are adsorbed at the surface of apatite nanodomains. They also can be included in the apatitic structure; nevertheless introduction of metallic cations in the apatitic structure is doubtful.

5. Conclusion

The synthesis of nanocrystallized phosphate–silicate calcium hydroxyapatite is possible by dissolution of natural minerals, precipitation in a basic aqueous solution and calcination at 900 °C for 1 h. This material contains 0.4 silicate groups per cell. A small quantity of carbonates is detected by global analysis and may be present in apatitic structure or in micro-inclusions. In addition, this material contains 1%wt spherical non-stoichiometric magnesioferrite nanoparticles.

Calcination has a very important role in synthesizing the final material; it removes B-type carbonates from the apatitic structure, enhances crystallization of the phosphate–silicate apatite and allows growth of magnesioferrite crystals by phase segregation.

This material allows the association of properties from phosphate–silicate apatites and magnesioferrite nanoparticles. This should open to several applications, such as medical magnetic biomaterials or as chemical barriers for the mediation of polluted soils or water.

Acknowledgements

The authors wish to thank SARIA Industries and ANRT association that financially supported this work. We would also like to thank the Aix-Marseille 3 University and CNRS for offering accesses to laboratory equipment and technical support.

References

[1] J.C. Elliott, Structure and Chemistry of the Apatite and Other Calcium Orthophosphates, Elsevier, Amsterdam, 1994.
[2] N.O. Engin, A.C. Tas, Manufacture of macroporous calcium hydroxyapatite bioceramics, J. Eur. Ceram. Soc. 19 (1999) 2569–2572.
[3] H. Narita, Y. Takeda, K. Takagaki, T. Nakamura, S. Harata, M. Endo, Identification of glycosaminoglycans using high-performance liquid chromatography on a hydroxyapatite column, Anal. Biochem. 232 (1) (1995) 133–136.
[4] M. Nagai, T. Nishimo, T. Saeki, A new type of carbon dioxide gas sensor comprising porous hydroxyapatite ceramics, Sensors Actuators 15 (2) (1998) 145–151.
[5] T.A. Ionannidis, A.I. Zouboulis, Detoxification of a highly toxic lead loaded industrial solid waste by stabilization using apatites, J. Hazard. Mater. B 97 (2003) 173–191.
[6] M.I. Domínguez, J. Carpena, D. Borschneck, M.A. Centeno, J.A. Odriozola, J. Rose, Apatite and Portland/apatite composite cements obtained using a hydrothermal method for retaining heavy metals, J. Hazard. Mater. 150 (2008) 99–108.
[7] J. Carpena, L. Boyer, J.L. Lacout, U.S. patent no. 6624339, 2001.
[8] S.F. Hulber, J.C. Bokros, L.L. Hench, J. Wilson, G. Heimke, Ceramics in clinical applications: past, present and future, in: P. Vincenzini (Ed.), High Tech Ceramics, Elsevier, Amsterdam, 1987, pp. 189–213.
[9] E.M. Carlisle, Silicon: a possible factor in bone calcification, Science 167 (1970) 279–280.
[10] J. Carpena, J.L. Lacout, French patent no. 93 08676, 1993.
[11] R. Bros, J. Carpena, V. Sere, A. Beltritti, Occurrence of Pu and fissiogenic REE in hydrothermal apatites from the fossil nuclear reactor 16 at Oklo (Gabon), Radiochim. Acta 74 (1996) 277–282.
[12] A.J. Ruys, Silicon-doped hydroxyapatite, J. Aust. Ceram. Soc. 29 (1993) 71–80.
[13] Y. Tanizawa, T. Suzuki, X-ray photoelectron spectroscopy study of silicate-containing apatite, Phosphorus Res. Bull. 4 (1994) 83–88.
[14] K. Sugiyama, T. Suzuki, T. Satoh, Bactericidal activity of silicate-containing apatite, J. Antibact. Antifung. Agents 23 (1995) 67–71.
[15] L. Boyer, J. Carpena, J.L. Lacout, Synthesis of phosphate-silicate apatites at atmospheric pressure, Solid State Ionics 95 (1997) 121–129.
[16] K.S. Leshkivich, E.A. Monroe, Solubility characteristics of synthetic silicate sulphate apatites, J. Mater. Sci. 28 (1993) 9–14.
[17] I.R. Gibson, S.M. Best, W. Bonfield, Chemical characterization of silicon-substituted hydroxyapatite, J. Biomed. Mater. Res. 44 (4) (1999) 422–428.
[18] M. Corno, C. Busco, B. Civalleri, P. Ugliengo, Periodic ab initio study of structural and vibrational features of hexagonal hydroxyapatite $Ca_{10}(PO_4)_6(OH)_2$, Phys. Chem. Chem. Phys. 8 (2006) 2464–2472.
[19] W.W. Chen, Y. Kinemuchi, T. Tamura, K. Miwa, K. Watari, Grain-oriented calcium hydroxyapatite ceramic and film prepared by magnetic alignment, Mater. Lett. 61 (2007) 6–9.
[20] N. Meenakshi Sundaram, E.K. Girija, M. Askoh, T.K. Anee, R. Vani, R.V. Suganthi, Crystallisation of hydroxyapatite nanocrystals under magnetic field, Mater. Lett. 60 (2006) 761–765.
[21] A. Nakahira, S. Konishi, F. Nishimura, M. Iwasaka, S. Ueno, Effect of a high magnetic field on the bioactivity of apatite-based biomaterials, J. Appl. Phys. 93 (2003) 8513–8515.
[22] D. Arcos, R.P. Del Real, M. Vallet-Regí, Biphasic materials for bone grafting and hyperthermia treatment of cancer, J. Biomed. Mater. Res. A 65 (2003) 71–78.
[23] J.L. Dormann, D. Fiorani, Magnetic Properties of Fine Particles, North Holland, Amsterdam, 1992.
[24] M. Badruzzaman, P. Westerhoff, D.R.U. Knappe, Intraparticle diffusion and adsorption of arsenate onto granular ferric hydroxide (GFH), Water Res. 38 (18) (2004) 4002–4012.
[25] H. Genç-Fuhrman, P.S. Mikkelsen, A. Ledin, Simultaneous removal of As, Cd, Cr, Cu, Ni, and Zn from stormwater: experimental comparison of 11 different sorbents, Water Res. 41 (3) (2007) 591–602.
[26] K.A. Gross, R. Jackson, J.D. Cashion, L.M. Rodriguez-Lorenzo, Iron substituted apatites : a resorbable biomaterial with potential magnetic properties, Eur. Cells Mater. 3 (2) (2002) 114–117.
[27] Y. Guo, Y. Zhou, D. Jia, Q. Meng, Fabrication and in vitro characterization of magnetic hydroxycarbonate apatite coatings with hierarchically porous structures, Acta Biomater. 4 (2008) 923–931.
[28] C.C. Silva, F.P. Filho, M.F.P. Graça, M.A. Valente, A.S.B. Sombra, Dielectrical and structural characterization of iron oxide added to hydroxyapatite, Bull. Mater. Sci. 31 (4) (2008) 635–638.
[29] M.E. Fleet, Infrared spectra of carbonate apatites: ν2-region bands, Biomaterials 30 (2009) 1473–1481.
[30] E. Herrero, M.V. Cabañas, M. Vallet-Regi, J.L. Martinez, J.M. Gonzalez-Calbet, Influence of synthesis conditions on the γ-Fe_2O_3 properties, Solid State Ionics 101–103 (1) (1997) 213–219.
[31] J.P. Wirtz, M.E. Fine, Superparamagnetic magnesioferrite precipitates from dilute solutions of iron in MgO, J. Appl. Phys. 38 (1967) 3729–3737.
[32] H.U. Worm, On the superparamagnetic: stable single domain transition for magnetite and frequency dependence of susceptibility, GJI 133 (1) (1998) 201–206.
[33] R.M. Wilson, S.E.P. Dowker, J.C. Elliott, Rietveld refinements and spectroscopic structural studies of a Na-free carbonate apatite made by hydrolysis of monetite, Biomaterials 27 (2006) 4682–4692.
[34] M.E. Fleet, X. Liu, Coupled substitution of type A and B carbonate in sodium-bearing apatite, Biomaterials 28 (2007) 916–926.
[35] A. Antonakos, E. Liarokapis, T. Leventouri, Micro-Raman and FTIR studies of synthetic and natural apatites, Biomaterials 28 (2007) 3043–3054.